CONDENSED MATTER PHYSICS

Decoupled ultrafast electronic and structural phase transitions in photoexcited monoclinic VO_2

Jiyu Xu[1]†, Daqiang Chen[1,2]†, Sheng Meng[1,2,3]*

Photoexcitation has emerged as an efficient way to trigger phase transitions in strongly correlated materials. There are great controversies about the atomistic mechanisms of structural phase transitions (SPTs) from monoclinic (M_1-) to rutile (R-) VO_2 and its association with electronic insulator-metal transitions (IMTs). Here, we illustrate the underlying atomistic processes and decoupling nature of photoinduced SPT and IMT in nonequilibrium states. The photoinduced SPT proceeds in the order of dilation of V-V pairs and increase of twisting angles after a small delay of ~40 fs. Dynamic simulations with hybrid functionals confirm the existence of isostructural IMT. The photoinduced SPT and IMT exhibit the same thresholds of electronic excitations, indicating similar fluence thresholds in experiments. The IMT is quasi-instantaneously (<10 fs) generated, while the SPT takes place with time a constant of 100 to 300 fs. These findings clarify some key controversies in the literature and provide insights into nonequilibrium phase transitions in correlated materials.

INTRODUCTION

Vanadium dioxide (VO_2) is one of the archetypal strongly correlated materials (*1*, *2*). It undergoes a first-order phase transition from the monoclinic (M_1) insulating phase to the rutile (R) metallic phase at $T_c \approx 340$ K (*3*). The charge, lattice, orbital, and spin degrees of freedom are strongly coupled together. The complex interactions of multiple degrees of freedom lead to various phase transition pathways of insulator-metal transition (IMT) in VO_2 (*4*–*7*), obscuring their underlying mechanisms. Photoexcitation via ultrafast laser pulses has emerged as an efficient route to trigger the phase transitions of strongly correlated materials (*8*–*10*). The intense laser pulses can suddenly change the potential energy surface (PES) of lattice via electronic excitations (*11*, *12*), which enables the nonthermal pathways for structural phase transition (SPT) of M_1-VO_2 within 500 fs (*13*, *14*). The ultrafast SPT from M_1-VO_2 to R-VO_2 is first demonstrated in ultrafast optical and x-ray diffraction measurements (*13*). Baum *et al.* (*14*) proposed the atomistic mechanisms of photoinduced SPTs from M_1-VO_2 to R-VO_2, including bond dilation, atomic displacements, and sound wave shear motions. However, the critical role of atomic disordering was also identified during photoinduced SPTs (*15*), and other complexities—e.g., doping, defects, and strain effects—lead to rather inhomogeneous behaviors (*16*, *17*). The atomistic mechanisms of SPT/IMT following photoexcitation commonly escape the direct experimental detections.

It remains highly controversial whether laser pulses can induce decoupled SPT and IMT in photoexcited nonequilibrium states (*5*, *9*, *11*, *18*–*23*). Early experiments emphasized the importance of lattice distortions in photoinduced IMT in VO_2 (*13*), while recent time-resolved experimental studies revealed the different time scales for IMTs and structural transformations following photoexcitation (*14*, *23*). Wegkamp *et al.* (*24*) observed the quasi-instantaneous transformation of M_1-VO_2 into a metal, while time-resolved electron diffraction usually shows the time scale of 100 to 500 fs for the dilation of V-V dimers of M_1-VO_2 (*15*, *17*, *25*). Morrison *et al.* (*25*) proposed the metal-like metastable state within the M_1 configuration, according to the fluence threshold difference in ultrafast electron diffraction and infrared transmissivity experiments. However, Vidas *et al.* (*26*) argued that the threshold difference can be attributed to heat accumulation in multimodal experiments; therefore, SPT and IMT is a single process. Key to these debates is accurate characterization of the nature and features (thresholds, time scales, etc.) for the photoinduced ultrafast SPT and IMT.

In this work, we perform extensive, accurate, real-time time-dependent density functional theory (rt-TDDFT) simulations to reveal the underlying mechanisms of photoinduced SPT and IMT in M_1-VO_2. The photoexcitation was found to trigger decoupled ultrafast SPT and IMT. Photoexcitation produces holes in the $d_{||}$ valence band, which initiates the dilation of V-V pairs and the increase of twisting angles, driving SPT from M_1-VO_2 to R-VO_2. The calculated SPT rates and thresholds are in good agreement with the available experimental data. The dynamic hybrid functional calculations confirm the emergence of isostructural IMT in M_1-VO_2 and the decoupled IMT and SPT dynamics. The hole-induced gap collapse in M_1-VO_2 occurs with the filling of interval energy levels and the upshift of $d_{||}$ band. The calculated thresholds of electronic excitations are nearly identical for SPT and IMT, indicating the same fluence thresholds in experiments. The transition times of SPT and IMT differ by hundreds of femtoseconds, confirming the existence of photoinduced short-lived isostructural metallic M_1-VO_2 transient.

RESULTS AND DISCUSSION

Atomic structures of VO_2

The low-temperature M_1-VO_2 phase (Fig. 1A) is characterized by the dimerization of V chains along the ***c*** axis of high-temperature R-VO_2 phase (Fig. 1B), leading to the doubling of unit cell volume. Compared to the V-V bond length $d_R = 2.88$ Å in R-VO_2, the dimerization leads to shorter and longer bond lengths $d_S = 2.47$ Å and $d_L = 3.17$ Å, while the zigzag patterns give rise to V-V-V twisting angle $\theta \approx 165°$ in M_1-VO_2. The calculated bandgap of ~0.7 eV

[1]Beijing National Laboratory for Condensed Matter Physics and Institute of Physics, Chinese Academy of Sciences, Beijing 100190, People's Republic of China. [2]School of Physical Sciences, University of Chinese Academy of Sciences, Beijing 100049, People's Republic of China. [3]Songshan Lake Materials Laboratory, Dongguan, Guangdong 523808, People's Republic of China.
*Corresponding author. Email: smeng@iphy.ac.cn
†These authors contributed equally to this work.

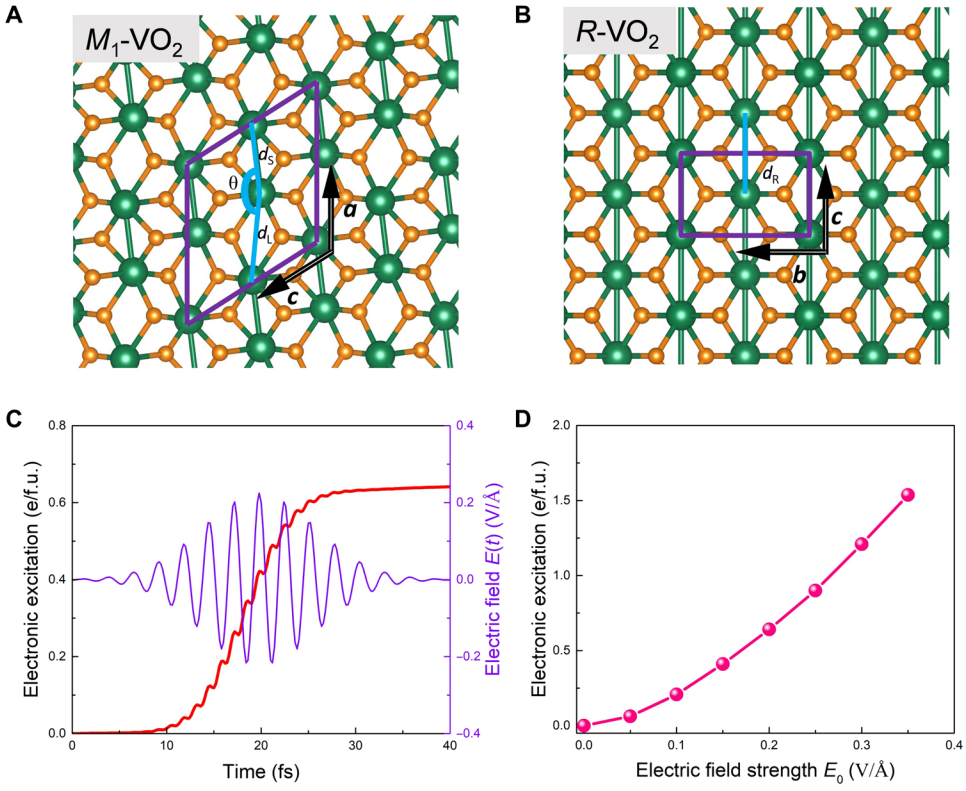

Fig. 1. The atomistic structure and photoinduced electronic excitation. The atomic configuration of low-temperature insulator M_1-VO_2 phase (**A**) and high-temperature metallic R-VO_2 phase (**B**). The vanadium and oxygen atoms are shown in green and orange, respectively. (**C**) Envelope of 800-nm laser pulses with the maximum electric field E_0 of 0.20 V/Å and the evolution of density of photoexcited holes ρ_h in M_1-VO_2. e/f.u., electrons per formula unit. (**D**) Final hole density ρ_h after photoexcitation as a function of maximum electric field strength E_0 of laser pulse.

(fig. S1A) for M_1-VO_2 is close to the experimental value of 0.6 eV (*2*), and the metallic R-VO_2 band structure is also reproduced (fig. S1B). The dimerization of V-V pairs and the Hubbard correction (U) jointly affect the IMT. The d-orbital bonding states of V-V pairs ($d_{||}$) lie right below the Fermi level, and the shift of $d_{||}$ band is strongly correlated with the IMT. The projected density of states analysis shows the dominant contributions of V d_{x2-y2} state to the $d_{||}$ band (fig. S1A).

Photoinduced ultrafast SPT

The photoinduced structural dynamics of M_1-VO_2 were simulated with nonadiabatic rt-TDDFT (*27*, *28*). After adequate equilibration to include disorder effects, the 2 × 2 × 2 supercell of M_1-VO_2 was irradiated with the laser pulse of $E(t) = E_0 \cos[2\pi(c/\lambda)t] \exp[-(t-t_0)^2/2\sigma^2]$ (Fig. 1C). We used the laser pulse with the wavelength λ = 800 nm and the width σ = 6 fs centered at t_0 = 20 fs, and the laser wavelength of 800 nm is consistent with experimental setups (*13*–*15*, *17*, *25*). The electric field $E(t)$ is along the ***a*** direction, and the maximum electric field strength E_0 ranges from 0.05 to 0.35 V/Å. The laser pulses (800 nm) excite the valence electrons at the $d_{||}$ band to the conduction band, inducing equivalent electron and hole doping in M_1-VO_2. The hole doping weakens the V-V short bonds (*29*), dominating the dilation of V-V pairs and the succeeding SPT processes (fig. S2, A to E). The effective electronic excitations were then defined by the density of photoexcited holes (ρ_h) at t = 40 fs (Fig. 1C). Figure 1D shows that ρ_h ranges from 0.06 to 1.54 electrons per formula unit (e/f.u.) for simulations with E_0 changing from 0.05 to 0.35 V/Å. For convenience, below, we use the density of excited holes instead of electric field strength of laser pulses to characterize the intensity of photoexcitation.

Both bond lengths and twisting angles can be used as the order parameters for the SPT from M_1-VO_2 to R-VO_2. Figure 2A shows the temporal evolution of average length of short bonds (d_S) and long bonds (d_L). The mean responses reflect well the ultrafast lattice dynamics responding to sudden change of PES (fig. S2), and the spreads from mean evolutions indicate the disorder effects from thermal fluctuations. For ρ_h > 0.5 e/f.u., the length of long bonds (d_L) and short ones (d_S) quickly transforms to d_R within the 260-fs-long simulations, indicating the ultrafast SPT from M_1-VO_2 to R-VO_2. Consistently, the twisting angle θ also undergoes the accompanying increase during corresponding electronic excitations (Fig. 2B), and the initiation of bond dilations (at $t \approx$ 30 fs) is ~40 fs earlier than that of the increase of twisting angles (at $t \approx$ 70 fs). The delay between dimer dilation and twisting angle increase is seemingly in accord with the two-step SPT mechanism (*14*), but the delay time is much smaller here. This small delay may be washed out in measurements considering current experimental accuracy. Figure 2C exhibits the decrease of charge density between V-V pairs at t = 40 fs, reflecting the excitations of $d_{||}$ band and the driving forces for the bond dilation. The photoexcited electrons are primarily located around individual V atoms.

The oscillations in bond lengths and twisting angles were observed at ρ_h = 0.90 e/f.u. (Fig. 2, A and B). The oscillations of

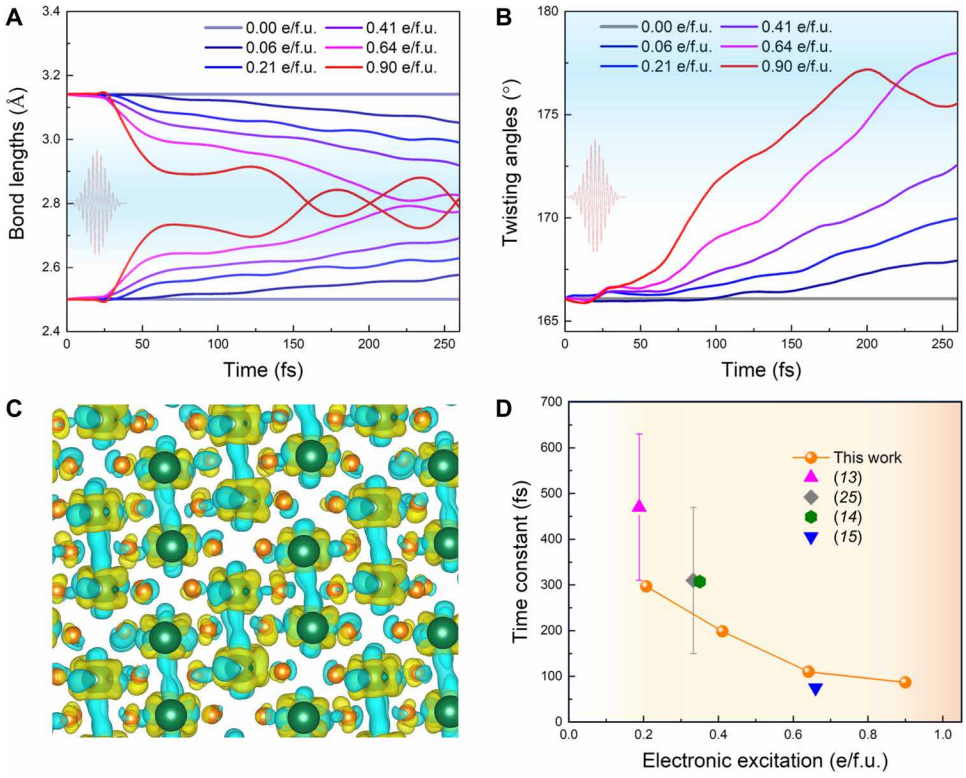

Fig. 2. The photoinduced ultrafast SPT from M_1-VO_2 to R-VO_2 in rt-TDDFT+U simulations. (**A**) Temporal evolution of average long bond lengths (d_L) and short ones (d_S) at different excitation densities. (**B**) Temporal evolution of average twisting angles θ. The light envelope is also shown in (A) and (B). (**C**) Photoinduced charge density difference at t = 40 fs after the photoexcitation of 0.64 e/f.u. The yellow region corresponds to electron increase, and the cyan region corresponds to electron decrease. (**D**) Time constant of SPT upon photoexcitation as compared with the available experimental data.

bond lengths are greatly amplified with intense photohole doping $\rho_h > 0.90$ e/f.u. (fig. S3A). Moreover, the twisting angle θ undergoes a rapid decrease after the initial increase (fig. S3B), and the effective atomic temperature increases by ~1000 K (fig. S3C). Therefore, the violent excitations destroy the lattice orders differing from both M_1-VO_2 and R-VO_2 phases and trigger the nonthermal melting to produce amorphous or damaged states (fig. S3D). The strong oscillations are attributed to laser-induced vibrations and the finite size effects. The vibration energies can be transferred to other degree of freedoms in realistic conditions. We note that the oscillations are different from coherent phonons observed in experiments, as coherent phonons are generated by laser pulses with fluences around threshold of phase transition (*11*, *12*). Previous experimental (*13*) and theoretical (*29*) works have demonstrated that the ultrafast SPT can be triggered with $\rho_h > 0.15$ e/f.u. In this case, the damage threshold of 0.90 e/f.u. is six times of the SPT threshold of 0.15 e/f.u., which is consistent with the fact that the damage thresholds are almost five to six times of that for SPT (*13*, *17*).

As the evolutions of bonds and twisting angles are nearly linear with time, we conducted linear extrapolations to obtain the finishing times of SPT for $\rho_h < 0.5$ e/f.u. The time constant of phase transition is then defined as half of the finishing times $[(t - t_0)/2]$. Figure 2D shows the simulated time constants of SPT with photohole doping. Electronic excitation of ρ_h = 0.06 e/f.u. can only slightly distort atomic configurations of M_1-VO_2 by modifying the PES (*29*). The time constants range from 300 to 100 fs for ρ_h = 0.21 to 0.90 e/f.u., and the severe excitations of $d_{||}$ band lead to the ultrafast SPT. To directly compare with experiments, here, we estimate the experimental ρ_h in available experiments by linear scaling with the electronic excitation for SPT threshold set to 0.15 e/f.u. (*13*–*15*, *25*). As shown in Fig. 2D, the simulated time constants show an excellent agreement with the available experimental data despite the slightly faster SPT rates at low electronic excitations. We note that experimental results suffer from limited time and structural resolutions due to instrumental responses, defects in samples, etc. The exact SPT rates are also affected by the random velocities of atoms (thermal fluctuations) besides the driving forces of laser pulses acting on atoms (*30*). Compared with ideal crystals studied in simulations, the complexities in real experiments may lead to nonmonotonic SPT rates (*16*, *17*). Theoretically, the SPT from M_1-VO_2 to R-VO_2 can be triggered by photohole doping ρ_h = 0.15 to 0.90 e/f.u., and the corresponding time constants of SPT range from 300 to 100 fs. The nonadiabatic ab initio simulations with TDDFT+U give a reasonable description of ultrafast SPT from M_1-VO_2 to R-VO_2.

Born-Oppenheimer molecular dynamics simulations with a fixed high electron temperature (T_e) were previously used to study the ultrafast SPT/IMT processes (*15*), and fixed T_e method combined with generalized Langevin dynamics was shown to describe well nonequilibrium evolutions of phonon modes in metallic systems (*31*). However, the constant electronic temperature T_e artificially introduces electronic excitations due to the gap closure along phase transition pathways (fig. S4) and accelerates SPT processes. The initiation of dimer dilation is subject to structural fluctuations, and the start times of dilation are more scattered in the early stage

(within ~100 fs). The broad distributions of bond lengths of the products may reflect the average of two phases (*15*) and are in notable contrast with those of stable *R*-VO_2 obtained at ρ_h = 0.64 e/f.u. in rt-TDDFT+*U* simulations (fig. S2A). The rt-TDDFT+*U* simulations demonstrate the direct structural transformations. Although the Ehrenfest dynamics simulation based on rt-TDDFT is a mean field approach, which uses the averaged PES of excited states, the electron-lattice coupling can be adequately treated because the photoexcited states here involve many electrons and many similar PESs in a small energy range. Thus, it is reasonable to average over all these excited-state PESs, which produce a driving force for the generation of specific phonon modes together. These simulations of coupled electron-lattice dynamics yield very good agreement with band structure evolution observed in angle-resolved photoelectron spectroscopy (*27*) and lattice structure evolution in ultrafast x-ray diffraction experiments (*32*). On the other hand, nonequilibrium electronic occupations are the intrinsic feature upon photoexcitation, and electronic thermalization times are close to the time constants of ultrafast SPT (fig. S5). Although it can be argued that rt-TDDFT simulations might not describe electronic thermalization processes accurately, we note that the obtained electron relaxation times are consistent with experimental measurements (*33*–*35*).

Photoinduced isostructural IMT

Because of the underlying Mott physics, the electronic occupation plays a critical role in the conductivity of M_1-VO_2, which cannot be accurately described by TDDFT+*U* (*36*). Hubbard *U*–independent methods are desirable to properly account for instantaneous electronic behaviors (*24*), and the Heyd-Scuseria-Ernzerhof (HSE06) (*37*, *38*) hybrid functional is used in our dynamic simulations. We first considered the hole doping effects by adjusting the T_e in M_1-VO_2 configurations, because modulating T_e naturally includes the hole doping effects (fig. S6A). Figure 3A shows the density of states (DOS) of M_1-VO_2 with hole doping, and the bandgap is ~1.4 eV for M_1-VO_2 without electronic excitations, consistent with previous values (*39*). The hole doping result in broadening and up-shift of $d_{||}$ band. The peak of $d_{||}$ band shift to −0.25 eV for ρ_h = 0.51 e/f.u. (fig. S6B), while the conduction bands exhibit minor shifts (Fig. 3A). Meanwhile, the bandgap collapses with hole doping. The obvious isostructural IMT is obtained with ρ_h > 0.2 e/f.u. (Fig. 3A), while the zoom-in view shows the IMT threshold of ~0.1 e/f.u. (Fig. 3A, inset). A similar threshold of ~0.08 e/f.u. was reported for IMT in GW calculations (*24*). In general, the threshold of IMT is very close to that of the SPT for VO_2. We note that the hole-induced up-shift of $d_{||}$ band is also predicted with DFT+*U* calculations (fig. S7), but the large

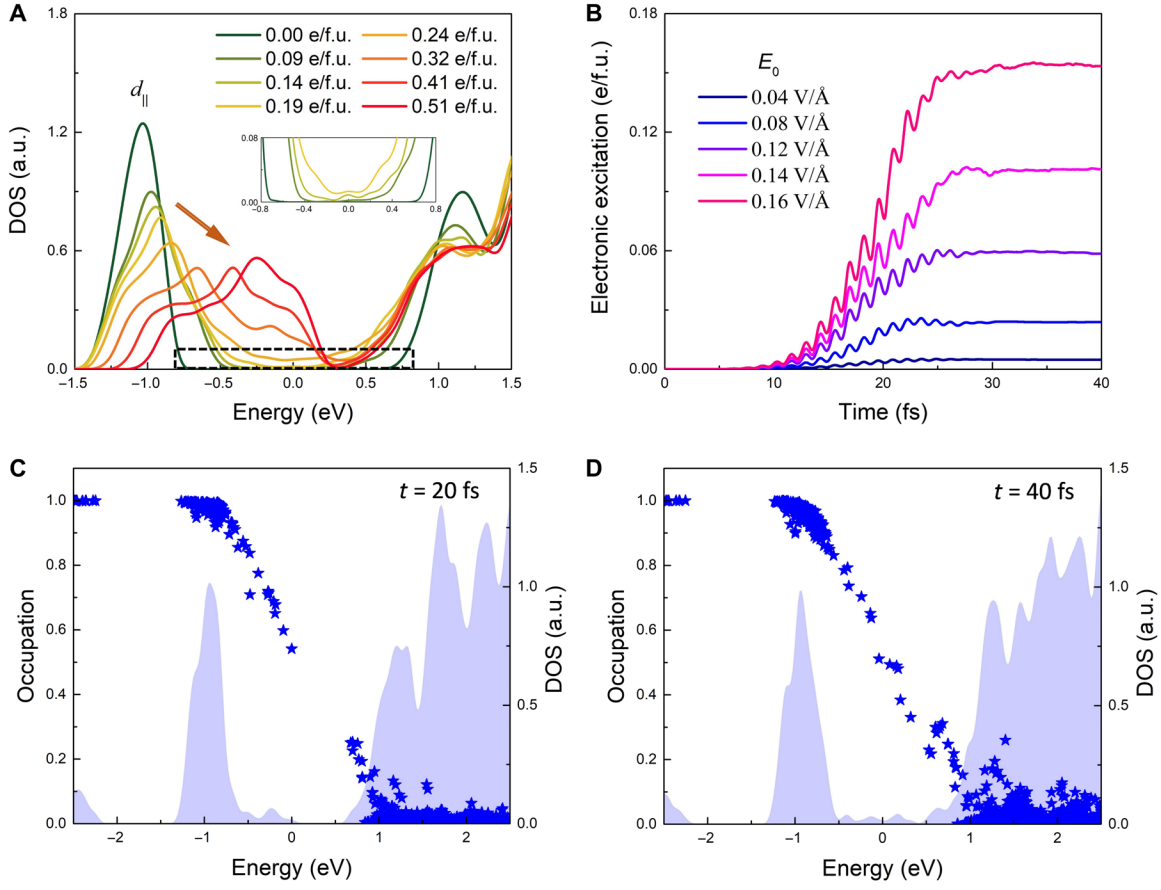

Fig. 3. The photoinduced isostructural IMT of M_1-VO_2 in rt-TDDFT simulations with hybrid functional. (**A**) DOS of M_1-VO_2 with electronic excitations in density functional theory (DFT) calculations with hybrid functional. The inset shows the zoom-in view of the dashed box in (A). a.u., arbitrary units. (**B**) Temporal evolutions of electronic excitations with maximum electric field strength E_0 of laser pulses in nonadiabatic hybrid functional simulations. The electronic occupations at *t* = 20 fs (**C**) and *t* = 40 fs (**D**) in the rt-TDDFT simulation with E_0 of 0.14 V/Å. The instantaneous DOS was also shown in (C) and (D).

threshold of ~0.4 e/f.u. calls for using a proper laser-modulated effective U (*36*).

Beyond the equilibrium simulations, the rt-TDDFT simulations with HSE06 functional were performed to directly track the photoinduced IMT and the decoupling between IMT and SPT at low electronic excitations. The conventional cell of M_1-VO_2 and the same laser pulses were used. Because there are no notable atomic motions during the first 40 fs at low electronic excitations (Fig. 2, A and B), all atoms were fixed during the 40-fs-long simulations with the hybrid functional. Figure 3B exhibits the temporal evolutions of electronic excitations with the maximum electric field E_0 in dynamic hybrid functional simulations. The intensity of electronic excitation is lower than those in TDDFT+U simulations because of the larger bandgap (fig. S8). Figure 3 (C and D) shows the electronic occupations at t = 20 fs and t = 40 fs in the simulations with E_0 = 0.14 V/Å, and the corresponding instantaneous hole doping is 0.05 and 0.10 e/f.u., respectively. The occupation variations demonstrate that the bandgap gradually collapses with the filling of interval energy levels at the threshold, and the peak of $d_{||}$ band exhibits small shifts in this regime (<0.2 e/f.u.) (fig. S6B). The filling effect is more prominent than that in equilibrium descriptions (Fig. 3A), reflecting the excitation and relaxation dynamics of nonequilibrium electronic subsystem. The obvious shifts of $d_{||}$ band peak dominate the gap closure at larger electronic excitation, and the critical role of hole doping was identified to reduce the electronic correlations (*18*). Nevertheless, the threshold is ~0.1 e/f.u. for isostructural IMT in dynamic hybrid functional simulations despite nonequilibrium distributions in electronic subsystems (Fig. 3D). The threshold for isostructural IMT is similar to that in T_e-dependent hybrid functional calculations (Fig. 3A).

The similar thresholds of electronic excitation for both SPT and IMT revealed here are consistent with the experimental measurements carefully characterizing the heating effects where a single threshold is observed for both SPT and IMT (*26*). A recent experimental work also demonstrated only one threshold for both the superstructure and nonsuperstructure peaks via well-separated diffraction spots of quasi–single-crystal VO_2 (*40*). Thus, both ultrafast SPT and IMT of VO_2 can be triggered with the same laser pulses, indicating the same fluence thresholds in experiments. However, the photoinduced SPT and IMT are characterized by different phase transition rates (Fig. 4). The IMT is quasi-instantaneously generated when the electronic excitation reaches the threshold (within 10 fs with E_0 of 0.14 V/Å), while the SPT occurs with the time constant of 100 to 300 fs. Consequently, the decoupling of IMT and SPT takes place following the photoexcitation of M_1-VO_2. The generated transient metallic states cannot be maintained within ideal M_1-VO_2 configurations and are limited to the time range of subpicoseconds. The time scales are consistent with the experimental observations that both IMT and SPT are finished within 1 ps (*26*), and the decoupling explains well the photoinduced constant electronic conductivity together with the obvious coherent phonon motions (*11*).

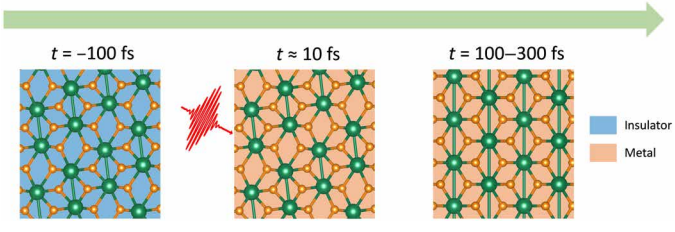

Fig. 4. The schematic for the photoinduced ultrafast electronic and structural dynamics in M_1-VO_2. The initial insulating M_1-VO_2 (t = −100 fs) is excited with the laser pulses centered at t = 0 fs. The photoexcitation induces the quasi-instantaneous IMT (within 10 fs) in M_1-VO_2 configuration, and the SPT occurs with the time delay of 100 to 300 fs. The blue and orange backgrounds correspond to the insulating and metallic states, respectively.

Previous studies proposed the photoinduced long-lived metallic M-VO_2 phase based on differences of fluence thresholds for SPT and IMT in multimodal experiments and the emergence of unique picosecond dynamics (*17*, *25*). The picosecond dynamics were explained as the reorganization of valence charge density and electrostatic potential, and the proposed metallic M-VO_2 exhibits antiferroelectric charge order without structural rearrangements (*17*). Here, we show that there is nearly no difference of excitation thresholds for photoinduced SPT and IMT of VO_2. Furthermore, our rt-TDDFT simulations demonstrate that the transient metallic states cannot be maintained to picosecond time scale within the ideal periodic M_1-VO_2 configurations. The possible picosecond dynamics may be attributed to the distinct excitation and relaxation dynamics originating from inhomogeneous behaviors of polycrystalline samples (*16*). For example, the heterogeneities of polycrystalline samples could result in the spatially varying T_c and fluence thresholds at the nanoscale (*21*), which may lead to the spatial heterogeneities of transition time at low excitation intensity (*41*). Furthermore, the metallic M phase was shown to be stabilized by local heterogeneities and interfacial interactions between equilibrium phases (*21*). It was also demonstrated that interfacial interactions stabilize a nonequilibrium metallic phase and lead to the isostructural IMT in epitaxial heterostructures of VO_2 (*18*). The excitation and relaxation of heterogeneous systems at longer time scales are beyond the scope of this work.

In conclusion, we unraveled the nature of photoinduced ultrafast SPT and IMT and demonstrated the decoupling of SPT and IMT at the subpicosecond time scale on the basis of extensive rt-TDDFT simulations. The ultrafast SPT is initiated by the excitation of valence electrons of the $d_{||}$ band and proceeds in the order of V-V pair dilations and twisting angle increases and with a small delay of ~40 fs. The simulated SPT rates and thresholds are well consistent with the available experimental data. The rt-TDDFT simulations with hybrid functional directly demonstrated the photoinduced isostructural IMT and the decoupling with SPT. The filling effects of interval energy levels lead to the IMT at the threshold, while the shifts of $d_{||}$ band peak dominate the gap closure at larger electronic excitation. The ultrafast SPT and IMT exhibit the same thresholds of electronic excitation, reflecting the same fluence thresholds in experiments. The decoupling of SPT and IMT features different phase transition rates and induces the generation of short-lived isostructural metallic M_1-VO_2 transient. This work exemplifies a new way to understand photoinduced nonequilibrium states in strongly correlated materials.

MATERIALS AND METHODS

Density functional theory calculations

The density functional theory (DFT) calculations including the Hubbard U corrections (DFT+U) were carried out using the Quantum ESPRESSO (*42*). The projector augmented wave (*43*) method and Perdew-Burke-Ernzerhof (*44*) exchange-correlation functional were used in the calculations. The wave functions and charge density

were represented by plane wave basis sets with energy cutoffs of 48 and 645 rydberg (Ry), respectively. The nonspin-polarized calculations are shown to describe well the nonmagnetic M_1-VO_2 (*45*, *46*) and paramagnetic R-VO_2 (*47*). The Hubbard U of 3.5 eV (*45*, *48*) for V 3d states was used, which gives the bandgap of ~0.7 eV for M_1-VO_2 (fig. S1A), consistent with the experimental value of 0.6 eV (*2*). The Brillouin zone was sampled with the 8 × 8 × 8 and 4 × 4 × 8 k-point meshes for M_1-VO_2 and R-VO_2, respectively. The convergent criterion of geometrical optimization was set to 3 meV/Å in structural optimizations. The obtained lattice constants of M_1-VO_2 are a = 5.60 Å, b = 4.61 Å, and c = 5.45 Å as well as β =121.70°, and the obtained lattice constants of R-VO_2 are a = 4.57 Å and c = 2.88 Å. Both agree well with the experimental lattice constants (*49*, *50*). Besides DFT+U calculations, we performed the hybrid functional calculations of M_1-VO_2 with Heyd-Scuseria-Ernzerhof (HSE06) (*37*, *38*) hybrid functional. We considered the photodoping effects of M_1-VO_2 by a convenient way of modulating T_e and calculated the corresponding DOS with a 15 × 15 × 15 k-point mesh. The input structure of M_1-VO_2 is from the DFT+U calculations. The optimized norm-conserving Vanderbilt pseudopotentials (*51*) and the plane wave energy cutoff of 85 Ry were used.

rt-TDDFT simulations

The rt-TDDFT simulations were performed via the Time Dependent Ab-initio Package (TDAP) implementations (*27*, *28*) in Quantum ESPRESSO (*42*). We simulated the photoinduced structural dynamics of M_1-VO_2 within the TDDFT+U protocols. A 2 × 2 × 2 supercell of M_1-VO_2 was used, and the atomic configuration was equilibrated for 3 ps at 300 K in NVT ensemble. The Brillouin zone was sampled with a 2 × 2 × 2 k-point mesh, and 160 unoccupied electronic states were considered. The time step for nuclei is 0.2 fs, and the time step for electrons is 0.2 as. The reliable description of electronic dynamics requires high-level calculations (*24*, *39*, *52*, *53*). Beyond TDDFT+U protocols, we also performed the rt-TDDFT simulations with the HSE06 (*37*, *38*) hybrid functional to accurately describe the electronic dynamics. The conventional cell of M_1-VO_2 was used, and all atoms are fixed during the simulations. The Brillouin zone was sampled with a 6 × 6 × 6 k-point mesh, and 20 unoccupied electronic states were considered. The other setups are consistent with the ground-state calculations. We used the laser pulse of $E(t) = E_0 \cos[2\pi(c/\lambda)t] \exp[-(t-t_0)^2/2\sigma^2]$ with the wavelength λ = 800 nm and the width σ = 6 fs centered at t_0 = 20 fs. The electric field $E(t)$ is along a-axis direction, and the maximum electric field E_0 ranges from 0.04 to 0.35 V/Å for the nonadiabatic simulations with TDDFT+U and HSE06 hybrid functional. The velocity gauge is used to enable the periodic electric fields in nonadiabatic simulations (*54*).

SUPPLEMENTARY MATERIALS

Supplementary material for this article is available at https://science.org/doi/10.1126/sciadv.add2392

REFERENCES AND NOTES

1. K. Liu, S. Lee, S. Yang, O. Delaire, J. Wu, Recent progresses on physics and applications of vanadium dioxide. *Mater. Today* **21**, 875–896 (2018).
2. Z. Shao, X. Cao, H. Luo, P. Jin, Recent progress in the phase-transition mechanism and modulation of vanadium dioxide materials. *NPG Asia Mater.* **10**, 581–605 (2018).
3. F. J. Morin, Oxides which show a metal-to-insulator transition at the Neel temperature. *Phys. Rev. Lett.* **3**, 34–36 (1959).
4. S. Kittiwatanakul, S. A. Wolf, J. Lu, Large epitaxial bi-axial strain induces a Mott-like phase transition in VO_2. *Appl. Phys. Lett.* **105**, 073112 (2014).
5. E. Arcangeletti, L. Baldassarre, D. Di Castro, S. Lupi, L. Malavasi, C. Marini, A. Perucchi, P. Postorino, Evidence of a pressure-induced metallization process in monoclinic VO_2. *Phys. Rev. Lett.* **98**, 196406 (2007).
6. S. Chen, Z. Wang, H. Ren, Y. Chen, W. Yan, C. Wang, B. Li, J. Jiang, C. Zou, Gate-controlled VO_2 phase transition for high-performance smart windows. *Sci. Adv.* **5**, eaav6815 (2019).
7. J. del Valle, N. M. Vargas, R. Rocco, P. Salev, Y. Kalcheim, P. N. Lapa, C. Adda, M.-H. Lee, P. Y. Wang, L. Fratino, M. J. Rozenberg, I. K. Schuller, Spatiotemporal characterization of the field-induced insulator-to-metal transition. *Science* **373**, 907–911 (2021).
8. M. Liu, H. Y. Hwang, H. Tao, A. C. Strikwerda, K. Fan, G. R. Keiser, A. J. Sternbach, K. G. West, S. Kittiwatanakul, J. Lu, S. A. Wolf, F. G. Omenetto, X. Zhang, K. A. Nelson, R. D. Averitt, Terahertz-field-induced insulator-to-metal transition in vanadium dioxide metamaterial. *Nature* **487**, 345–348 (2012).
9. D. Wegkamp, J. Stähler, Ultrafast dynamics during the photoinduced phase transition in VO_2. *Prog. Surf. Sci.* **90**, 464–502 (2015).
10. T. L. Cocker, L. V. Titova, S. Fourmaux, G. Holloway, H.-C. Bandulet, D. Brassard, J.-C. Kieffer, M. A. El Khakani, F. A. Hegmann, Phase diagram of the ultrafast photoinduced insulator-metal transition in vanadium dioxide. *Phys. Rev. B* **85**, 155120 (2012).
11. C. Kübler, H. Ehrke, R. Huber, R. Lopez, A. Halabica, R. F. Haglund Jr., A. Leitenstorfer, Coherent structural dynamics and electronic correlations during an ultrafast insulator-to-metal phase transition in VO_2. *Phys. Rev. Lett.* **99**, 116401 (2007).
12. S. Wall, D. Wegkamp, L. Foglia, K. Appavoo, J. Nag, R. F. Haglund Jr., J. Stähler, M. Wolf, Ultrafast changes in lattice symmetry probed by coherent phonons. *Nat. Commun.* **3**, 721 (2012).
13. A. Cavalleri, C. Tóth, C. W. Siders, J. A. Squier, F. Ráksi, P. Forget, J. C. Kieffer, Femtosecond structural dynamics in VO_2 during an ultrafast solid-solid phase transition. *Phys. Rev. Lett.* **87**, 237401 (2001).
14. P. Baum, D.-S. Yang, A. H. Zewail, 4D visualization of transitional structures in phase transformations by electron diffraction. *Science* **318**, 788–792 (2007).
15. S. Wall, S. Yang, L. Vidas, M. Chollet, J. M. Glownia, M. Kozina, T. Katayama, T. Henighan, M. Jiang, T. A. Miller, D. A. Reis, L. A. Boatner, O. Delaire, M. Trigo, Ultrafast disordering of vanadium dimers in photoexcited VO_2. *Science* **362**, 572–576 (2018).
16. B. T. O'Callahan, A. C. Jones, J. H. Park, D. H. Cobden, J. M. Atkin, M. B. Raschke, Inhomogeneity of the ultrafast insulator-to-metal transition dynamics of VO_2. *Nat. Commun.* **6**, 6849 (2015).
17. M. R. Otto, L. P. René de Cotret, D. A. Valverde-Chavez, K. L. Tiwari, N. Émond, M. Chaker, D. G. Cooke, B. J. Siwick, How optical excitation controls the structure and properties of vanadium dioxide. *Proc. Natl. Acad. Sci. U.S.A.* **116**, 450–455 (2019).
18. D. Lee, B. Chung, Y. Shi, G.-Y. Kim, N. Campbell, F. Xue, K. Song, S.-Y. Choi, J. P. Podkaminer, T. H. Kim, P. J. Ryan, J.-W. Kim, T. R. Paudel, J.-H. Kang, J. W. Spinuzzi, D. A. Tenne, E. Y. Tsymbal, M. S. Rzchowski, L. Q. Chen, J. Lee, C. B. Eom, Isostructural metal-insulator transition in VO_2. *Science* **362**, 1037–1040 (2018).
19. Z. Tao, T.-R. T. Han, S. D. Mahanti, P. M. Duxbury, F. Yuan, C.-Y. Ruan, K. Wang, J. Wu, Decoupling of structural and electronic phase transitions in VO_2. *Phys. Rev. Lett.* **109**, 166406 (2012).
20. Z. Li, J. Wu, Z. Hu, Y. Lin, Q. Chen, Y. Guo, Y. Liu, Y. Zhao, J. Peng, W. Chu, C. Wu, Y. Xie, Imaging metal-like monoclinic phase stabilized by surface coordination effect in vanadium dioxide nanobeam. *Nat. Commun.* **8**, 15561 (2017).
21. A. Sood, X. Shen, Y. Shi, S. Kumar, S. J. Park, M. Zajac, Y. Sun, L.-Q. Chen, S. Ramanathan, X. Wang, W. C. Chueh, A. M. Lindenberg, Universal phase dynamics in VO_2 switches revealed by ultrafast operando diffraction. *Science* **373**, 352–355 (2021).
22. X. Fu, F. Barantani, S. Gargiulo, I. Madan, G. Berruto, T. LaGrange, L. Jin, J. Wu, G. M. Vanacore, F. Carbone, Y. Zhu, Nanoscale-femtosecond dielectric response of Mott insulators captured by two-color near-field ultrafast electron microscopy. *Nat. Commun.* **11**, 5770 (2020).
23. M. F. Jager, C. Ott, P. M. Kraus, C. J. Kaplan, W. Pouse, R. E. Marvel, R. F. Haglund, D. M. Neumark, S. R. Leone, Tracking the insulator-to-metal phase transition in VO_2 with few-femtosecond extreme UV transient absorption spectroscopy. *Proc. Natl. Acad. Sci. U.S.A.* **114**, 9558–9563 (2017).
24. D. Wegkamp, M. Herzog, L. Xian, M. Gatti, P. Cudazzo, C. L. McGahan, R. E. Marvel, R. F. Haglund, A. Rubio, M. Wolf, J. Stähler, Instantaneous band gap collapse in photoexcited monoclinic VO_2 due to photocarrier doping. *Phys. Rev. Lett.* **113**, 216401 (2014).
25. V. R. Morrison, R. P. Chatelain, K. L. Tiwari, A. Hendaoui, A. Bruhács, M. Chaker, B. J. Siwick, A photoinduced metal-like phase of monoclinic VO_2 revealed by ultrafast electron diffraction. *Science* **346**, 445–448 (2014).
26. L. Vidas, D. Schick, E. Martínez, D. Perez-Salinas, A. Ramos-Álvarez, S. Cichy, S. Batlle-Porro, A. S. Johnson, K. A. Hallman, R. F. Haglund Jr., S. Wall, Does VO_2 host a transient monoclinic metallic phase? *Phys. Rev. X* **10**, 031047 (2020).
27. C. Lian, S.-J. Zhang, S.-Q. Hu, M.-X. Guan, S. Meng, Ultrafast charge ordering by self-amplified exciton–phonon dynamics in $TiSe_2$. *Nat. Commun.* **11**, 43 (2020).
28. J. Xu, D. Chen, S. Meng, Probing laser-induced plasma generation in liquid water. *J. Am. Chem. Soc.* **143**, 10382–10388 (2021).

29. X. Yuan, W. Zhang, P. Zhang, Hole-lattice coupling and photoinduced insulator-metal transition in VO_2. *Phys. Rev. B* **88**, 035119 (2013).
30. X. Wang, J. C. Ekström, Å. U. J. Bengtsson, A. Jarnac, A. Jurgilaitis, V.-T. Pham, D. Kroon, H. Enquist, J. Larsson, Role of thermal equilibrium dynamics in atomic motion during nonthermal laser-induced melting. *Phys. Rev. Lett.* **124**, 105701 (2020).
31. A. Tamm, M. Caro, A. Caro, G. Samolyuk, M. Klintenberg, A. A. Correa, Langevin dynamics with spatial correlations as a model for electron-phonon coupling. *Phys. Rev. Lett.* **120**, 185501 (2018).
32. C. Lian, S. B. Zhang, S. Meng, Ab initio evidence for nonthermal characteristics in ultrafast laser melting. *Phys. Rev. B* **94**, 184310 (2016).
33. W. S. Fann, R. Storz, H. W. K. Tom, J. Bokor, Direct measurement of nonequilibrium electron-energy distributions in subpicosecond laser-heated gold films. *Phys. Rev. Lett.* **68**, 2834–2837 (1992).
34. M. Obergfell, J. Demsar, Tracking the time evolution of the electron distribution function in copper by femtosecond broadband optical spectroscopy. *Phys. Rev. Lett.* **124**, 037401 (2020).
35. B. Rethfeld, D. S. Ivanov, M. E. Garcia, S. I. Anisimov, Modelling ultrafast laser ablation. *J. Phys. D Appl. Phys.* **50**, 193001 (2017).
36. N. Tancogne-Dejean, M. A. Sentef, A. Rubio, Ultrafast modification of Hubbard *U* in a strongly correlated material: Ab initio high-harmonic generation in NiO. *Phys. Rev. Lett.* **121**, 097402 (2018).
37. J. Heyd, G. E. Scuseria, M. Ernzerhof, Hybrid functionals based on a screened Coulomb potential. *J. Chem. Phys.* **118**, 8207–8215 (2003).
38. A. V. Krukau, O. A. Vydrov, A. F. Izmaylov, G. E. Scuseria, Influence of the exchange screening parameter on the performance of screened hybrid functionals. *J. Chem. Phys.* **125**, 224106 (2006).
39. V. Eyert, VO_2: A novel view from band theory. *Phys. Rev. Lett.* **107**, 016401 (2011).
40. C. Xu, C. Jin, Z. Chen, Q. Lu, Y. Cheng, B. Zhang, F. Qi, J. Chen, X. Yin, G. Wang, D. Xiang, D. Qian, VO_2 does not host a photoinduced long-lived monoclinic metallic phase. arXiv:2203.09776 [cond-mat.mtrl-sci] (18 March 2022).
41. A. S. Johnson, D. Pérez-Salinas, K. M. Siddiqui, S. Kim, S. Choi, K. Volckaert, P. E. Majchrzak, S. Ulstrup, K. Hallman, R. F. Haglund Jr., C. M. Günther, B. Pfau, S. Eisebitt, D. Backes, F. Maccherozzi, A. Fitzpatrick, S. Dhesi, P. Gargiani, M. Valvidares, H. Choi, D. Jang, A. Katoch, S. Kwon, S. H. Park, H. Kim, S. E. Wall, Ultrafast X-Ray hyperspectral imaging of a photo-induced phase transition with nanometer space and femtosecond time resolution. arXiv:2202.08585 [cond-mat.str-el] (17 February 2022).
42. P. Giannozzi, S. Baroni, N. Bonini, M. Calandra, R. Car, C. Cavazzoni, D. Ceresoli, G. L. Chiarotti, M. Cococcioni, I. Dabo, A. D. Corso, S. de Gironcoli, S. Fabris, G. Fratesi, R. Gebauer, U. Gerstmann, C. Gougoussis, A. Kokalj, M. Lazzeri, L. Martin-Samos, N. Marzari, F. Mauri, R. Mazzarello, S. Paolini, A. Pasquarello, L. Paulatto, C. Sbraccia, S. Scandolo, G. Sclauzero, A. P. Seitsonen, A. Smogunov, P. Umari, R. M. Wentzcovitch, QUANTUM ESPRESSO: A modular and open-source software project for quantum simulations of materials. *J. Phys. Condens. Matter* **21**, 395502 (2009).
43. P. E. Blöchl, Projector augmented-wave method. *Phys. Rev. B* **50**, 17953–17979 (1994).
44. J. P. Perdew, K. Burke, M. Ernzerhof, Generalized gradient approximation made simple. *Phy. Rev. Lett.* **77**, 3865–3868 (1996).
45. C. Sun, L. Yan, B. Yue, H. Liu, Y. Gao, The modulation of metal–insulator transition temperature of vanadium dioxide: A density functional theory study. *J. Mater. Chem. C* **2**, 9283–9293 (2014).
46. T. A. Mellan, H. Wang, U. Schwingenschlögl, R. Grau-Crespo, Origin of the transition entropy in vanadium dioxide. *Phys. Rev. B* **99**, 064113 (2019).
47. T. A. Mellan, R. Grau-Crespo, Density functional theory study of rutile VO_2 surfaces. *J. Chem. Phys.* **137**, 154706 (2012).
48. B. Y. Qu, H. Y. He, B. C. Pan, The dynamical process of the phase transition from VO_2(M) to VO_2(R). *J. Appl. Phys.* **110**, 113517 (2011).
49. J. M. Longo, P. Kierkegaard, A refinement of the structure of VO_2. *Acta Chem. Scand.* **24**, 420–426 (1970).
50. D. B. McWhan, M. Marezio, J. P. Remeika, P. D. Dernier, X-ray diffraction study of metallic VO_2. *Phys. Rev. B* **10**, 490–495 (1974).
51. D. R. Hamann, Optimized norm-conserving Vanderbilt pseudopotentials. *Phys. Rev. B* **88**, 085117 (2013).
52. W. H. Brito, M. C. O. Aguiar, K. Haule, G. Kotliar, Metal-insulator transition in VO_2: A DFT+DMFT perspective. *Phys. Rev. Lett.* **117**, 056402 (2016).
53. H. Zheng, L. K. Wagner, Computation of the correlated metal-insulator transition in vanadium dioxide from first principles. *Phys. Rev. Lett.* **114**, 176401 (2015).
54. C. Lian, M. Guan, S. Hu, J. Zhang, S. Meng, Photoexcitation in solids: First-principles quantum simulations by real-time TDDFT. *Adv. Theory Simul.* **1**, 1800055 (2018).

Acknowledgments

Funding: We acknowledge financial support from the Ministry of Science and Technology (no. 2021YFA1400201), the National Natural Science Foundation of China (nos. 12025407 and 11934004), and the Chinese Academy of Sciences (no. YSBR047 and XDB330301). **Author contributions:** J.X. and S.M. conceived the project. J.X. performed the DFT calculations and nonadiabatic rt-TDDFT simulations and analyzed the data. D.C. implemented the modules of rt-TDDFT codes. J.X. and S.M. wrote the paper. **Competing interests:** The authors declare that they have no competing interests. **Data and materials availability:** All data needed to evaluate the conclusions in the paper are present in the paper and/or the Supplementary Materials.

Submitted 30 May 2022
Accepted 16 September 2022
Published 4 November 2022
10.1126/sciadv.add2392